Title

A High-Content Screen Identifies Drugs That Restrict Tumor Cell Extravasation across the Endothelial Barrier

Journal

Cancer Research, 81(3)

ISSN

0008-5472

Authors

Hilfenhaus, Georg
Mompeón, Ana
Freshman, Jonathan
et al.

Publication Date

2021-02-01

DOI

10.1158/0008-5472.can-19-3911

Peer reviewed

HHS Public Access

Author manuscript

Cancer Res. Author manuscript; available in PMC 2021 August 01.

Published in final edited form as:

Cancer Res. 2021 February 01; 81(3): 619–633. doi:10.1158/0008-5472.CAN-19-3911.

A high-content screen identifies drugs that restrict tumor cell extravasation across the endothelial barrier

Georg Hilfenhaus[1], **Ana Mompeón**[2], **Jonathan Freshman**[1], **Divya P. Prajapati**[1], **Gloria Hernandez**[3], **Vanessa M. Freitas**[4], **Feiyang Ma**[3], **Adam D. Langenbacher**[1], **Snezana Mirkov**[2], **Dana Song**[1], **Byoung-Kyu Cho**[5], **Young Ah Goo**[5], **Matteo Pellegrini**[1,3], **Jau-Nian Chen**[1,3], **Robert Damoiseaux**[6,7,8], **M. Luisa Iruela-Arispe**[1,2,3,8]

[1]Department of Molecular, Cell and Developmental Biology, University of California, Los Angeles, CA 90095

[2]Department of Cell and Developmental Biology, Feinberg School of Medicine, Northwestern University, Chicago, IL 60611.

[3]Molecular Biology Institute, University of California, Los Angeles, CA 90095

[4]Department of Cell and Developmental Biology, Institute of Biomedical Sciences, University of São Paulo, São Paulo, Brazil

[5]Proteomics Center of Excellence, Feinberg School of Medicine, Northwestern University, Chicago, IL 60611.

[6]Department of Molecular and Medical Pharmacology, University of California, Los Angeles, CA 90095

[7]California NanoSystems Institute, University of California, Los Angeles, CA 90095

[8]Jonsson Comprehensive Cancer Center, University of California, Los Angeles, CA 90095

Abstract

Metastases largely rely on hematogenous dissemination of tumor cells via the vascular system and significantly limit prognosis of patients with solid tumors. To colonize distant sites, circulating tumor cells must destabilize the endothelial barrier and transmigrate across the vessel wall. Here we performed a high-content screen to identify drugs that block tumor cell extravasation by testing 3520 compounds on a transendothelial invasion co-culture assay. Hits were further characterized and validated using a series of in vitro assays, a zebrafish model enabling 3-D visualization of tumor cell extravasation, and mouse models of lung metastasis. The initial screen advanced 38 compounds as potential hits, of which 4 compounds enhanced endothelial barrier stability while concurrently suppressing tumor cell motility. Two compounds niclosamide and forskolin significantly reduced tumor cell extravasation in zebrafish, and niclosamide drastically impaired metastasis in mice. Because niclosamide had not previously been linked with effects on barrier

*Please address correspondence to: M. Luisa Iruela-Arispe, Ph.D., 303 E. Superior st. SQ 8-522, Northwestern University, Chicago, IL 60611, arispe@northwestern.edu, Phone: 312-503-7958.

R. Damoiseaux is a consultant to Amgen, Holoclara, Panorama Medicine, Acurastem and is co-founder/owns stock in Forcyte and EnspireBio. All other authors declare no potential conflicts of interest.

function, single cell RNA sequencing uncovered mechanistic effects of the drug on both tumor and endothelial cells. Importantly, niclosamide affected homotypic and heterotypic signaling critical to intercellular junctions, cell-matrix interactions, and cytoskeletal regulation. Proteomic analysis indicated that niclosamide-treated mice also showed reduced levels of kininogen, the precursor to the permeability mediator bradykinin. Our findings designate niclosamide as an effective drug that restricts tumor cell extravasation through modulation of signaling pathways, chemokines, and tumor-endothelial cell interactions.

Keywords

compound screening; forskolin; metastasis; niclosamide; tumor cell extravasation; vascular

Introduction

Distant metastasis frequently transforms a localized and potentially curable tumor disease into an extensive multifocal pathology with limited therapeutic options (1). In fact, for some cancers, like pancreatic cancer, the high incidence of distant metastasis is in large part responsible for poor prognosis (2). Newly diagnosed patients with solid tumors are at constant risk of metastatic disease either prior to or during the tumor resection procedure (3,4). The vascular system is the primary route for tumor cells to spread to distant organs (5). After entering the circulation, tumor cells must survive a hostile intravascular environment where they are exposed to mechanical shear stress and immune surveillance (6). Once physically restricted in small capillaries, tumor cells form attachments with the endothelium, destabilize the endothelial barrier, transmigrate and implant into the adjacent extravascular tissue (5,7,8).

The vascular endothelium forms a dynamic and highly selective barrier that tightly regulates the trafficking of circulating cells between the intravascular and extravascular compartments (8,9). While immune cells are equipped with a specialized machinery to easily transmigrate across the endothelium, circulating tumor cells are larger and apply less evolutionarily conserved steps to overcome the vascular barrier (7,8). Amongst those, transcellular diapedesis and tumor cell-induced endothelial cell death have been reported (10,11), in addition to paracellular transmigration through disruption of endothelial cell-cell junctions (7,8,12,13). Thus, the dynamic regulation of biomechanical structures such as intercellular junctions, cell-matrix adhesions, and cytoskeletal organization in both tumor cells and the endothelium, as well as heterotypic cross-talk between both cell types, are of particular importance for the extravasation step (12,14,15).

The contribution of the endothelial barrier to tumor cell extravasation has been underscored by different gain- and loss-of-function studies (7,8). These experiments highlighted critical roles for VE-cadherin and tight junctions (16,17), as well as endothelial Tie1, Tie2, and Notch1 (18–20). Understanding these molecular mechanisms provide a platform to exploit blockade of tumor cell extravasation through the enhancement of vascular barrier stability (21–23). While many of these studies have offered proof of principle, they have not significantly expanded the repertoire of drugs to target specific steps in the metastatic

cascade (24). Here, we performed a high-content screen using a transendothelial invasion co-culture assays to identify compounds that hinder tumor cell extravasation. Hits were further characterized using a series of *in vitro* assays, a zebrafish model that enables 3-D visualization of direct tumor cell-endothelium interactions, and two distinct mouse models of lung metastasis. Finally, single-cell sequencing and proteomics were used to gain mechanistic insights of drug effects on endothelial cells and shed light on their impact to the process of metastasis.

Materials and Methods

Cell lines

Human umbilical vein endothelial cells (HUVECs; Lonza, #C2519A) were cultured in MCDB-131 endothelial growth medium (VEC Technologies). The human pancreatic cancer cell lines PaTu-8902 (ACC-179) and MIA PaCa-2 (CRL-1420™) were a gift from Dr. Doug Hanahan (EPFL, Switzerland); 4T1 (CRL-2539™) and LLC1 (CRL-1642™) were purchased from ATCC. All tumor cell lines were cultured in DMEM (Gibco). Both types of culture media were supplemented with 10% fetal bovine serum (FBS; Omega Scientific). Prior to injection into mice, cell lines were also tested for mycoplasm and evaluated for pathogens (Charles River Laboratories).

Animals

BALB/cJ and C57BL/6 adult (8–10 weeks) mice were purchased from Jackson Laboratory (000651 and 000664). All experiments were previously approved and performed in accordance to NIH guidelines and Northwestern University IACUC. Zebrafish experiments were performed according to approved institutional animal care and use committee protocols at UCLA.

Lentiviral vectors, particle production and transduction

Lentiviral vectors (CMV-FP-IRES-puromycin) were used to express enhanced blue fluorescent protein (EBFP), green fluorescent protein (GFP), and red fluorescent protein (RFP) in endothelial and tumor cells. Generation of lentiviral particles and transduction of cells was performed as described (25).

Transendothelial tumor cell invasion assay and high-content screening

For 3-D surface renderings of transendothelial tumor cell invasion, EBFP-labeled HUVECs were plated onto gelatin-coated 8-wells (100,000 cells / well; Ibidi, #80826). After 48 hours, GFP-labeled PaTu-8902 (50,000 cells / well) were added onto HUVECs. Confocal microscopy was done following 1, 8, and 24 hours post co-culture. For high-content screening, compounds or DMSO (vehicle control) were plated with MCDB-131 medium (30 μL / well) into 384-wells (Greiner bio-one, #781091) using a multi-mode dispenser (MultiFlo FX, BioTek), and a pin-tool (Biomek FX automated workstation, Beckman Coulter). Positive control CN03 was purchased from Cytoskeleton, Inc. (#CN03). EBFP-labeled HUVECs (5,000 cells in 40 μL / well) were added and cultured with compounds at 5 μM for 40 hours, then GFP-labeled tumor cells were added onto the confluent endothelial monolayers (2,000 cells for PaTu-8902, or 1,000 cells for MIA PaCa-2, both delivered in 30

µL / well). Fluorescence imaging was performed every 24 hours using the ImageXpress MicroXL (Molecular Devices). Dose-response of selected compounds was tested at 18 concentrations (50 µM to 0.76 nM). Total EBFP- and GFP-positive areas were automatically determined using the MetaXpress analysis software (Molecular Devices, version 6.2.2.707). A total of 3520 compounds from LOPAC^{1280}, Prestwick Chemical Library, and NIH Clinical Collection, were screened. Compounds with a z-score of ≥ 4.0 or ≤ −4.0 for the EBFP-positive area 72 hours after the addition of tumor cells were considered as initial hits and were further validated in triplicate. The data was then analyzed by hierarchical clustering, including EBFP- and GFP-positive areas and all 4 imaging timepoints.

Tumor cell proliferation assays

Compounds, or DMSO (vehicle control), were plated with MCDB-131 medium into 384-well microplates. Subsequently, PaTu-8902 (750 cells / well) or MIA PaCa-2 (200 cells / well) were added. Final treatment concentration of test compounds was 1.0 µM and 5.0 µM. After 72 hours, viable cells were quantified using CellTiter-Glo according to manufacturer instructions (Promega, #G7572).

Zebrafish tumor cell extravasation model

Tg(kdrl:GFP)^{la116} transgenic zebrafish embryos (26) were used as described (27). 48 hours post-fertilization (hpf) zebrafish larvae were dechorionated, anesthetized with 160 µg/mL tricaine (Sigma-Aldrich), and positioned in wedged-shaped troughs of a 1.5% agarose pad. RFP-labeled PaTu-8902 were injected into the duct of Cuvier (approx. 100 cells in 5 nL PBS) using a microinjection system (pico-injector, PLI-100, Harvard Apparatus) under a stereo microscope (SZX12, Olympus). Intravascular tumor cell load of freshly injected fish embryos was graded into high/medium and low (fluorescence microscopy). Embryos with equivalent numbers of tumor cells were randomized into treatment groups and exposed to compounds or DMSO at a range of dosages (prior dose-response analysis) to assess possible toxic effects and a dose around the EC50 was selected for evaluation of metastasis. After 30 hours of incubation at 33 °C, zebrafish were transferred into a 384-well format, anesthetized, and placed into a confocal high-content imaging system (ImageXpress Micro Confocal, Molecular Devices). Z-stack confocal imaging was performed by imaging of 9 tiles (488 nm and 561 nm; 10X objective). Tiles were stitched and cropped using MetaXpress image analysis software, and color-merged z-stack files of the zebrafish embryos were generated. Number of intra- and extravascular tumor cells were obtained in the intersegmental vessels using Imaris.

Single-cell sequencing of tumor-endothelial cell co-cultures

Cultures of PaTu-8902 (375,000 cells) and HUVECs (200,000 cells), alone or as co-cultures (PaTu-8902 cells onto HUVEC monolayers), previously exposed to either 1.0 µM niclosamide or DMSO were isolated after 8 hours. For the generation of single-cell GEMs, 5200 suspended cells were loaded on a Chromium Single Cell Instrument (10x Genomics) per sample. Single-cell RNAseq libraries were prepared using the Chromium Single Cell 3’ Library & Gel Bead Kit v2 (10x Genomics). Sequencing was performed on Illumina HiSeq2500, and the digital expression matrix was generated by de-multiplexing, barcode processing and gene UMI (unique molecular index) counting using the Cell Ranger v2.1.1

pipeline (10x Genomics). Transcriptional analysis was performed using the R (Seurat). Cells that expressed less than 100 genes or 500 transcripts were eliminated, and 2000 variable genes were selected by Seurat for further analysis. The data was regressed by sequencing depth to remove unwanted source of variation. Principal component analysis (PCA) and uniform manifold approximation and projection (UMAP) were used to reduce the dimensionality of the data. A graph-based clustering approach was later used, and cell types were defined for each cluster using signature genes. Endothelial or tumor cell identity was defined by expression of either *CDH5* and *PECAM1,* or *EPCAM* and *KRT18*. For the ligand receptor analysis, the genes were first filtered by an average expression of 0.01 normalized counts. Ligand receptor pairs were collected from the iTALK database (28). The pair was considered differentially regulated if at least one gene (ligand or receptor) was differentially expressed. The scRNA-seq data were deposited in the GEO database (accession number: GSE160915).

Determination of niclosamide EC50 values

Cells were exposed to 6 concentrations (0.1 μg/ml to 3.2 μg/ml) of niclosamide or vehicle (5% EtOH, 10% DMSO, 30% cremophor, 55% HBSS) in 48-well plates and the impact of drug on tumor cell proliferation was evaluated for 96 hours. Plates were transferred to the IncuCyte Live-Cell Analysis System (Sartorius), images were acquired every hour and evaluated (IncuCyte analysis software). Concentration-response curves were generated and the half maximal effective concentration (EC50) values of niclosamide were determined at 96 hours (Graph Pad Prism).

Tumor metastasis mouse models

Two distinct sygeneic models were used based on the well-known metastatic abilities of 4T1 mammary cancer cells and Lewis lung carcinoma (LLC) cells. Both male and female mice between 10–14 weeks were used and total body weight was obtained prior initiating, and at time of termination. Tumor weight was also obtained (in the case of 4T1). Cells were expanded and always freshly plated 24 hours prior to injection. Four hours prior to trypsinization, cultures were washed and incubated in serum-free media to remove FBS, then trypsinized and counted. Trypsin was inactivated by soybean trypsin inhibitor (Thermo Fisher Scientific). For 4T1 cells, a total of 500,000 cells were injected subcutaneously on the right flank of BALBc mice. Upon implantation, 4T1 cells formed solid tumors, palpable by day 7 as a firm mass. Two weeks post implantation, animals were randomized for treatment. Intraperitoneal administration of niclosamide (20mg/kg/day) or vehicle control (10% DMSO, 55% HBSS, 30% cremophor, 5% ethanol) was performed daily intraperitoneally. Tumor growth was monitored and mice were sacrificed 4 weeks after injection. For LLC metastasis assays, a suspension consisting of 500,000 cells in 100ul of DMEM was injected intravenously (tail vein) in C57Bl6J mice. Niclosamide (20mg/kg/day) or vehicle control were administered intraperitoneally according to the trial. Three different trials were conducted: (1) Prevention trial (niclosamide or vehicle was injected 4 days prior tumor cell injection), (2) Intervention trial (treatment was initiated the day after tumor cell injection for 7 days) and (3) Prevention + Intervention trial (continuous treatment starting 4 days prior tumor cell injection and continued for 7 days after tumor cell injection). All trials terminated 4 weeks after the initial tumor injection. Blood was collected for proteomics and

metabolomics at the end of the experiment. Subsequently, mice were perfused in the right ventricle with 2% paraformaldehyde (PFA) followed by intratracheal injection of low melting agarose (1%) containing 2% PFA. Tissue was fixed overnight in 2% PFA and washed 4–5 times with PBS the next day. Specimens were either embedded in paraffin (left lobes and solid tumors) or in 7% agarose for vibratome sectioning (right lobe). For quantification of tumor metastasis, two blinded investigators counted the entire left lobe of each mouse (12–16 sections each at 400 μm). After decoding, the numbers were compared and found to be within 90–95% overlap. Data were plotted and significance assessed by t-test.

Tracer injection and evaluation of permeability

Alexa Fluor cadaverine-555 (1kDa) and dextran-FITC (10kDa) (Invitrogen) were injected iv at 10ug/g and allowed to circulate for 2 hrs. Mice were anesthetized and perfused with 10mls of HBSS. Tissues were removed, homogenized in lysis buffer, suppernatans were centrifuged 13,000rpm for 20min and fluorescence was measured on a fluorometer Synergy HT271167 plate reader. Results were normalized for total protein.

Immune cell quantification

Mice were perfused with DMEM to remove circulating blood. Lung and tumors were dissected and washed in DMEM. Tissue was minced and enzymatically digested following manufacture protocol (Miltenyi lung tissue dissociation kit, 130–095-927). Single-cell suspensions were then lysed with RBC lysis buffer (ThermoFisher 00–4333-57). Final single-cell suspension was stained with CD45-APCY7 (Biolegend, 103116), GR1-PB (Biolegend, 108430), CD11b-PE (BD, 552850), CD-19-FITC (Biolegend, 152404), CD3-APC (Biolegend, 100236), and Dapi(live/dead) on ice and then analyzed on BD FORTESSA. Cells were gated on DAPI negative, CD45+ and further defined as monocytes ($Gr^{lo}CD11b^{+}$, $CD3^{-}CD19^{-}$), granulocytes ($Gr^{hi}CD11b^{+}$, $CD3^{-}CD19^{-}$), T cells ($CD3^{+}$) and B cells ($CD19^{+}$).

Proteomics by liquid chromatography tandem mass spectrometry (LC-MS/MS)

Sample preparation: Mouse plasma protein concentration was measured by a BCA assay (Pierce BCA Protein Assay Kit, Thermo Fisher Scientific, Waltham, MA). 1 mg each was subjected to highly abundant protein depletion by Proteome Purify 2 Mouse Serum Protein Immunodepletion Resin (R&D Systems, Minneapolis, MN) following the manufacturer's protocol. Protein was concentrated and purified by acetone / trichloroacetic acid precipitation overnight at −20 °C. After washing the pellet with ice-cold acetone, resulting protein pellet was resuspended in 50 μL 8 M urea in 400 mM ammonium bicarbonate, pH 7.8, reduced with 4 mM dithiothreitol at 50 °C for 30 min, and cysteines were alkylated with 18 mM iodoacetamide for 30 min. The solution was then diluted to < 2 M urea and trypsin (Promega, Madison, WI) was added at final trypsin/protein ratio of 1:50 prior to overnight incubation at 37 °C. The resulting peptides were desalted using solid phase extraction on a Pierce C18 Spin column and eluted in 80 μl of 80% acetonitrile in 0.1% formic acid. After lyophilization, peptides were reconstituted with 5% acetonitrile in 0.1% formic acid.

Data acquisition and processing: Peptides were analyzed by LC-MS/MS using a Dionex UltiMate 3000 Rapid Separation nanoLC and a Q Exactive™ HF Hybrid Quadrupole-Orbitrap™ Mass Spectrometer (Thermo Fisher Scientific Inc, San Jose, CA). Approximately 1 μg of peptide samples was loaded onto the trap column of 3 μm C18 beads. The analytical column was a 75 μm x 10.5 cm PicoChip column packed with 3 μm C18 beads (New Objective, Inc. Woburn, MA). Flow rate was kept at 300nL/min. Solvent A was 0.1% FA in water and Solvent B was 0.1% FA in ACN. Peptides were separated on 120-min analytical gradient from 5% ACN/0.1% FA to 40% ACN/0.1% FA. The top 20 most abundant precursor ions in each MS^1 scan were selected for fragmentation. Precursors were selected with an isolation width of 2 Da and fragmented by Higher-energy collisional dissociation *(HCD)* at 30% normalized collision energy in the HCD cell. Previously selected ions were dynamically excluded from re-selection for 20 seconds. The MS^2 AGC was set to 1×10^5. All samples were run in duplicate.

Metabolomics

Plasma was immediately mixed with cold 80% methanol at a 10:1 ratio and incubated overnight. Subsequently samples were centrifuged at 20,000g for 30min at 4C. The metabolite-containing supernatant was then transferred to an Eppendorf. The protein pellet was used for total protein quantification. Extraction solution was dried using SpeedVac. 50% acetonitrile was added to the tube for reconstitution following by overtaxing for 30 sec. Sample solution was then centrifuged for 30 min at 20,000g, 4°C. Supernatant was collected for LCMS analysis. Samples were analyzed by High-Performance Liquid Chromatography and High-Resolution Mass Spectrometry and Tandem Mass Spectrometry (HPLC-MS/MS). Specifically, system consisted of a Thermo Q-Exactive in line with an electrospray source and an Ultimate3000 (Thermo) series HPLC consisting of a binary pump, degasser, and auto-sampler outfitted with a Xbridge Amide column (Waters; dimensions of 2.3 mm × 100 mm and a 3.5 μm particle size). The automatic gain control (AGC) target was set at 1×10^6 and the maximum injection time was 200 ms. The top 5 precursor ions were subsequently fragmented, in a data-dependent manner, using the higher energy collisional dissociation (HCD) cell set to 30% normalized collision energy in MS2 at a resolution power of 17,500. Besides matching m/z, metabolites are identified by matching either retention time with analytical standards and/or MS2 fragmentation pattern. Data acquisition and analysis were carried out by Xcalibur 4.1 software and Tracefinder 4.1 software, respectively (both from Thermo Fisher Scientific).

Statistical and computational data analysis

All analyses were performed using Prism (v8.0.2; GraphPad Software) unless otherwise indicated. P-values <0.05 were considered significant. Data are presented as means ± SEM or SD as indicated. Differences between groups were evaluated using ANOVA followed with Tukey's post-hoc multiple comparison test. Data pairs were compared by using a Student unpaired two-tailed t-test and Mann-Whitney test. The Z'-factor (screening window coefficient) of the screening assay was calculated using the formula $Z' = 1 - [(3\sigma_{c+} + 3\sigma_{c-})/|\mu_{c+} - \mu_{c-}|]$ (where σ: standard deviation, μ: mean, c+: positive control, c-: negative control). Hierarchical clustering of screening hits was performed in R using the heatmap.2 function. For correlation analyses, Spearman correlation coefficient (r_s) and slope were determined.

EC50 values were calculated using the nonlinear regression dose-response equation in Prism. Functional annotation cluster enrichment analyses were performed in DAVID v6.8 (https://david.ncifcrf.gov).

Protein Tandem MS data was queried for protein identification and label-free quantification against the SwissProt Mus musculus database using MaxQuant v1.6.0.16 (29). The following modifications were set as search parameters: peptide mass tolerance at 6 ppm, trypsin digestion cleavage after K or R (except when followed by P), 2 allowed missed cleavage site, carbamidomethylated cystein (static modification), and oxidized methionine, protein N-term acetylation (variable modification). Search results were validated with peptide and protein FDR both at 0.01. Proteins that were identified with >1 peptide were subjected to a further statistical analysis using Perseus software (version 1.6.0.7; 30,31). Catalog numbers for reagents and RRID were included in the Supplementary Materials.

Results

A high-content screening assay to identify inhibitors of tumor cell extravasation

In hematogenous metastasis of solid tumors, such as pancreatic cancer, extravasation of circulating tumor cells requires multiple interactions with the endothelium (7,8) (Fig. 1 A). Drugs targeting one or multiple steps could be effective inhibitors of tumor cell extravasation, and thus restrict distant metastasis. Using human pancreatic cancer cells (PaTu-8902 and MIA PaCa-2; Fig. S1 A), we developed a high-content screening assay based on the ability of these cells to disrupt endothelial monolayers. In fact, when plated onto a confluent monolayer of HUVECs, tumor cells adhere to the endothelium and progressively disrupt the endothelial barrier through invasive protrusions and cell expansion within a 24-hour time frame (Fig. 1 B). To automate the process in a 384-well format, we used EBFP-labeled endothelial cells (HUVECs) and GFP-labeled tumor cells (PaTu-8902 and MIA PaCa-2) treated either with test compounds or DMSO (vehicle control; Fig. 1 C). When unable to invade, tumor cells remained rounded in shape. In contrast, once tumor cells successfully overcame the endothelial barrier, they attached and spread, dislodging endothelial cells. This resulted in a larger GFP-positive area, and defects in the total EBFP-positive endothelial cell monolayer (Fig. 1 D). The two tumor cell lines used, PaTu-8902 and MIA PaCa-2, represent a wide range of pancreatic cancer phenotypes. While PaTu-8902 displayed an epithelial phenotype, both in regard to cell shape and expression of epithelial markers; MIA PaCa-2 exhibited a mesenchymal-like phenotype (Fig. S1 A and B). The recombinant protein CN03, which blocks GTPase activity by deamidation of Rho Gln-63 (32) and improves endothelial barrier stability (33), was used as a positive control. CN03 prevented tumor cell invasion and restored the integrity of the HUVEC monolayer (Fig. 1 D; and Fig. S1 C). For computational quantification, total areas of EBFP-positive endothelial cells and GFP-positive tumor cells were determined using fluorescence intensity thresholding. The area of EBFP-positive HUVECs was reduced by both PaTu-8902 and MIA PaCa-2 72 hours after the addition of tumor cells, and mostly unaffected when endothelial monolayers were pretreated with CN03 (Fig. 1 E, and Fig. S1 D). Evaluation of the GFP-positive area covered by either PaTu-8902 or MIA PaCa-2 (Fig. 1 F, and Fig. S1 E) provided a complementary rea-out. The suitability of the established assay for high-content

screening was validated by determination of a Z'-factor (screening window coefficient) of 0.653 for PaTu-8902, and 0.693 for MIA PaCa-2, respectively (29).

High-content screen identifies multiple compounds able to interfere with transendothelial tumor cell invasion

A high-content screening and validation pipeline was established to identify novel compounds that impaired transmigration of tumor cells (Fig. 2 A). As part of the workflow, initial hits were validated by dose-response, effects on tumor cell proliferation, endothelial barrier function, and tumor cell motility. Subsequently, promising compounds were evaluated *in vivo* using zebrafish and mouse models. A total of 3520 compounds (LOPAC^{1280} Library, Prestwick Chemical Library, and NIH Clinical Collection) were tested using both PaTu-8902 and MIA PaCa-2 cell lines (Fig. 2, A–C). Hits with inhibitory effects on transendothelial invasion were defined by a z-score of ≥ 4.0 of the total EBFP-positive area, as they only permitted limited disruption to HUVEC monolayers (Fig. 2 D, and Fig. S2 A). In contrast, hits promoting transendothelial invasion were identified by a z-score of ≤ −4.0 (EBFP-positive area). A hierarchical clustering analysis combined alterations in endothelial and tumor cell area, in triplicate and across both tumor cell types and four different timepoints, validated 55 compounds (Fig. 2 E). Of these, 38 inhibited and 17 promoted transendothelial tumor cell invasion. Validated hits showed different levels of effectiveness as per quantified area changes for HUVEC, and PaTu-8902 and MIA PaCa-2, respectively (Fig. 2 F; Fig. S2 B–D). Correlation of findings for PaTu-8902 and MIA PaCa-2 uncovered significant agreement on transendothelial invasion for both tumor cell lines, despite their broadly distinct phenotypes (Fig. 2 G).

Evaluation by drug categories, tumor cell proliferation, and dose-response analysis designates 14 compounds with favorable properties

The subset of compounds with inhibitory properties on transendothelial invasion encompased several drug categories (Fig. 3 A). Three of these, namely antimetabolites, topoisomerase inhibitors, and tubulin modulators, are also part of a broader group of antineoplastic agents. Because our main interest was on the enhancement of endothelial barrier, and/or suppression of tumor cell-endothelium interactions, we sought to exclude compounds with substantial effects on tumor cell proliferation. From the 38 compounds evaluated, 19 displayed substantial inhibition of tumor cell proliferation with a largely similar impact on both PaTu-8902 and MIA PaCa-2 (Fig 3 B). The combinatorial effects on transendothelial invasion and tumor cell proliferation by compound and associated drug category are shown in Fig. 3 C. As expected, most compounds that were part of the classical antineoplastic drug categories had a substantial impact on tumor cell proliferation and were excluded from further validation analyses. Hence, we selected 19 compounds with no or minor impact on tumor cell proliferation. These were subjected to further dose-response evaluation by using 18 different concentrations (50 μM to 0.76 nM). Fourteen of these compounds showed favorable EC50 values at or below 10 μM (Fig. 3 D) and were continued through the pipeline.

Candidate compounds promote endothelial barrier stability and cytoskeletal organization, and reduce tumor cell motility

The impact of the 14 candidate compounds on endothelial barrier stability was further assessed on established HUVEC monolayers (Fig. S3 A) by using electric cell-substrate impedance sensing (ECIS). Five of the 14 compounds, namely forskolin, niclosamide, dipyridamole, DMH4, and edelfosine elevated baseline resistance levels by 218.4 ± 22.6, 143.0 ± 22.9, 102.9 ± 22.4, 94.4 ± 38.3, and 66.0 ± 13.8 ohms above control, respectively (absolute resistance of control was 1,286.4 ohms; $P < 0.05$; Fig. S3 B). Importantly, we also measured transendothelial resistance after challenging endothelial monolayers with tumor cells (Fig. S3 A, C). Two compounds, forskolin and niclosamide, significantly diminished PaTu-8902-mediated loss of barrier resistance by 435.5 ± 39.3 and 311.2 ± 54.0 ohms compared to DMSO control, respectively (absolute resistance of control was 975.8 ohms; $P < 0.05$), indicating a strong barrier stabilizing effect.

As previously recognized (15,25), cortical organization of the actin cytoskeleton is required for the stability of the endothelial barrier; while stress fibers are frequently associated with low barrier tightness. To assess how the 14 candidate compounds affected actin fiber organization as a surrogate for barrier stability, HUVEC monolayers were treated with the different compounds and effects on actin cytoskeleton organization, as well as on migration were also evaluated (Fig. S3 D–J). While DMSO-treated HUVEC monolayers showed randomly distributed stress fibers, compounds like forskolin, niclosamide and atorvastatin induced reorganization of the cortical actin cytoskeleton, reflected by a significantly higher percentage of cells that were automatically detected by their actin fiber outlines (60.4 ± 2.8, 58.7 ± 1.4, and 57.1 ± 5.2 versus 35.0 ± 2.5 percent of cells in DMSO control; $P < 0.05$; Fig. S3 E; Fig. S4 A).

Next, the effect of candidate compounds on tumor cell motility was determined using scratch assays. Due to the different phenotype of each tumor line used for the study, we evaluated migration for the less invasive tumor cell line PaTu-8902 (no additional matrix), and invasion for the more aggressive tumor cell line MIA PaCa-2 (Fig. S3 F; and Fig. S4 B). The extent of tumor cell motility was determined by the percentage of the initial scratch area covered with migrating or invading tumor cells at 12 hours, or 48 hours, respectively. For PaTu-8902 the compounds methylbenzethonium chloride, forskolin, itraconazole, josamycin, niclosamide, and mupirocin significantly reduced tumor cell migration at 12 hours (51.2 ± 4.0, 72.7 ± 5.2, 76.7 ± 3.7, 79.0 ± 5.2, 86.7 ± 3.6, and 88.3 ± 4.0, versus 97.2 ± 1.9 percent relative scratch density for DMSO control; $P < 0.05$; Fig. S3 G, H). For MIA PaCa-2, a significant reduction of tumor cell invasion was observed when cells were exposed to niclosamide and diphenyleneiodonium chloride (12.8 ± 2.2 and 21.6 ± 3.4, versus 36.2 ± 4.3 percent relative scratch density for DMSO control; $P < 0.05$; Fig. S3 I,J). To eliminate interference of proliferation on the migration read-outs, experiments were also performed in the presence of cell cycle inhibitors (Fig. S4 C,D). For all *in vitro* experiments shown, optimal compound dosages were applied (see Fig. 3 D).

Niclosamide and forskolin significantly reduced tumor cell extravasation *in vivo*

From the 14 compounds characterized *in vitro*, four outperformed the rest on endothelial barrier and tumor cell motility (Fig. 4 A). Forskolin, niclosamide, dipyridamole, and atorvastatin exhibited robust ability to block tumor cell invasion of endothelial monolayers at low dosages. To test these compounds *in vivo,* and monitor their impact on tumor cell extravasation in real time, we tood advantage of the unique features of zebrafish (Fig. 4 B). PaTu-8902 were directly injected into the duct of Cuvier of *Tg(kdrl:GFP)*^{la116} zebrafish embryos two days post fertilization (dpf). After injection, fish were immediately exposed to the four candidate compounds or DMSO at optimal dosages above the EC50 concentration as determined by dose-response analysis. 3-D fluorescence imaging was performed at 30 hours, and the percentage of tumor cells present in the extravascular or intravascular compartments of intersegmental vessels was determined using Imaris imaging software (Fig. S5 A). Evaluation of multiple compounds in a larger number of treated zebrafish embryos was achieved by incorporating a confocal high-content imaging system as part of the validation workflow (Fig. S5 B). In comparison to the DMSO-treated control group, treatment with niclosamide or forskolin significantly decreased the percentage of extravasated tumor cells per zebrafish (mean fold change 0.757 ± 0.05, and 0.770 ± 0.07 of DMSO control, respectively; Fig. 4, C and D). No significant effect was observed with atorvastatin or dipyridamole. In the group of DMSO-treated zebrafish an average of 40.75 ± 2.1% PaTu-8902 were extravasated 30 hours post tumor cell injection. As forskolin is a well-known modulator of barrier function (34), we continued mechanistic studies using niclosamide as our top molecule.

Niclosamide modulates complex gene networks and ligand-receptor interactions critical for tumor cell extravasation

Single-cell RNA sequencing was used to explore mechanistic effects of niclosamide on tumor cell extravasation and endothelial barrier properties. Niclosamide-treated co-cultures were compared to co-cultures exposed to DMSO and to monocultures of PaTu-8902 and HUVECs (Fig. 5 A; and Fig. S6 A, B). Using these 3 different conditions, we were able to identify transcriptional changes reflective of tumor-endothelial cell contact (co-culture effect), and niclosamide treatment, on both tumor and endothelial cells. UMAP analysis of the obtained single-cell sequencing dataset identified distinct cell clusters of HUVEC and PaTu-8902, in each experimental condition (Fig. 5 B). Endothelial cell and tumor cell identity were confirmed by the expression of the markers *CDH5* and *PECAM1*, or *EPCAM* and *KRT18*, respectively (Fig. 5 C). Heatmaps of genes with most significant changes of RNA expression levels per condition and cell type are shown in Fig. 5, D and E. Of interest, the chemokines *CCL2* and *CXCL2*, as well as the inhibitor of DNA binding proteins *ID1* and *ID3*, were significantly upregulated upon tumor-endothelial cell contact, and downregulated by niclosamide treatment. In addition, niclosamide treatment significantly reduced transcripts of *MMP2* and *VWF* in tumor cells. Enrichment analysis of genes upregulated by tumor-endothelial cell contact highlighted inflammatory gene annotations such as NF-kB-, TNF-signaling, and CXC chemokines, as well as cell-cell junctions and cytoskeletal regulation (Fig. 5 F). Importantly, the top annotations modified by niclosamide were cell-cell adhesion and cell-cell junctions for both endothelial and tumor cells. The specific genes of these top clusters are shown in Fig. S6, C and D, and include cytoskeleton

and transmembrane proteins involved in stabilizing barrier function for endothelial cells, and promoting cell-cell attachment for tumor cells.

Further analyses using the iTALK database to highlight ligand-receptor interactions affecting either heterotypic (tumor and endothelial cells) or homotypic (endothelial-endothelial cells; tumor-tumor cells) changes were also performed (Fig. 5, G–H). Interaction pairs were considered differentially up- or down-regulated when at least one gene (ligand or receptor) was differentially expressed upon niclosamide treatment. Functional annotation of up- or down-regulated ligand-receptor genes identified a number of enriched clusters related to attachment, extracellular matrix, and cytoskeletal regulation, such as the top enriched clusters “focal adhesion, ECM organization, actin cytoskeletal regulation”, and “ECM organization, focal adhesion”, respectively (Fig. 5 G). In addition, the circos plot illustration of all down-regulated ligand-receptor interactions part of the top annotation cluster revealed the central role of integrin beta-1 (*ITGB1*) based on its numerous connections to other extravasation-related molecules (Fig. 5 H; circos plot of top up-regulated annotation genes see Fig. S6 E).

Niclosamide blocks metastasis in mouse models

Given the impact of niclosamide on the endothelial barrier, we further tested the compound on metastasis using immunocompetent models. Mouse mammary carcinoma cell line 4T1 was injected subcutaneously in BALB c mice and allowed to grow for two weeks, at which time mice were treated with either vehicle or niclosamide (intervention trial; Fig. 6 A). Due to the short stability of niclosamide at 37°C (Fig. S7 A–C) mice were injected daily. The number of metastatic nodules was determined on serial vibratome sections of the right lung lobe (Fig. S7 D,E). Evaluation of the data showed a statistically significant difference between vehicle and niclosamide-treated mice, despite little differences on the size of primary tumors or body weight (Fig. 6, B–D). There was no difference in the response of male or female mice to the treatment.

We also tested the efficacy of niclosamide in Lewis lung carcinoma (LLC) colonization. Because LLC cells were directly injected in the circulation, the model enabled prevention trials to address the question as to whether niclosamide could tighten vascular barrier prior to injection of tumor cells and prevent tumor seeding. Thus, we conducted both prevention and intervention trials (Fig. 6 E). In addition to counting the right lobe using vibratome sections, the left lung lobes were evaluated by histology. Differences in the presence and size of cancer nodules were evident by naked eye (Fig. 6, F–H). Detailed quantification was performed by counting metastatic nodules in vibratome sections of the entire left lobe in all animals, as done for the 4T1 experiments. The evaluation was carried out in blinded counts by two individuals with a 90% overlap in accuracy. The findings indicated that all three niclosamide treatment regimes resulted in a substantial reduction of metastatic disease (Fig. 6, I–K).

Niclosamide limits permeability but does not impair immune cell extravasation

Our results on endothelial barrier using electrical impedance analyses (Fig. S4 A) suggested niclosamide might restrict permeability *in vivo*. To address this question directly, we

performed permeability assays using tracers and immunocytochemical evaluation of fibrinogen, a plasma protein in tumor-bearing mice. We noted significant accumulation of fibrinogen in the extracellular space of the tumors in vehicle-treated, in contrast to low levels in niclosamide-treated animals (Fig. 7 A). Intravenous injection of cadaverin (1K) and dextran (10K) tracers followed by assessment of their leakage into the extravascular space showed that niclosamide significant prevented permeability in the lungs of tumor-bearing mice (Fig. 7, B and C). Importantly, niclosamide did not affect trafficking of immune cells, as determined by FACS and immunocytochemistry in the tumors or lungs of 4T1-injected mice (Fig. 7, D–F).

We also interrogated possible effects (and biomarkers) of niclosamide treatment by evaluating plasma proteins and metabolites in tumor-free and tumor-bearing mice. Proteomics analyses revealed multiple proteins affected by exposure to niclosamide in tumor-naïve mice (Fig. 7 G). Several proteins altered in tumor-free mice were also affected in tumor-bearing mice. One of these, kininogen, was further validated in tumor-bearing mice by immunoblots because of its relevance in the generation of bradykinin, a potent permeability mediator. Importantly, we noticed a signicant reduction of bradykinin in the plasma of tumor-bearing mice that were treated with niclosamide (Fig. 7 H). Metabolomics analyses of plasma were also performed in tumor-free (Fig. 7 I and J) and tumor-bearing mice (Fig. 7 K and L). The findings showed overlap in three metabolites: D-gluconic acid, pyruvic acid and alpha-ketoglutarate which could serve as potential indicators of niclosamide response in clinical trials, as they correlate with increased barrier post niclosamide treatment.

Discussion

Tumor cell extravasation is a complex process regulated by the metastatic phenotype of circulating tumor cells and their molecular interactions with the vascular endothelium. The importance of endothelial barrier integrity in this context has been long established and concur that tightening the vascular barrier prevents metastatic events (7,8). Unfortunately, previous studies are yet to translate this knowledge into clinical practice. Moreover, while in recent years specific targets on either tumor cells or the endothelium have been tested (21,22), the complexity of direct and indirect tumor-endothelial interactions and the efficacy of drugs with dual cell-specific effects have been neglected. Our work takes advantage of an unbiased screening approach of tumor-endothelial cell co-cultures, which initially advanced 38 compounds as potential hits for a more comprehensive characterization *in vitro*. From these, 4 compounds were selected for further evaluation in a zebrafish model that enables expeditious 3-D visualization of tumor cell extravasation through a high-content imaging system. Two compounds, niclosamide and forskolin, significantly reduced tumor cell extravasation *in vivo*. Finally, prevention and intervention trials in mice underscored the effect of niclosamide in preventing hematogenous metastasis. Mechanistically, single-cell sequencing was used to reveal drug effects on tumor and endothelial cell signaling, and the interaction network between both cell types in systems treated with niclosamide. Our findings identify niclosamide as an effective drug to restrict tumor cell extravasation, and mechanistically link its effect to modulation of cell signaling and heterotypic cross-talk

critical for intercellular junctions, cell-matrix interactions, permeability cytokines, and cytoskeletal regulation.

Approved in 1982 by the Food and Drug Administration as an anti-helminthic drug, niclosamide has been recently explored for other therapeutic purposes (35). In relation to cancer, niclosamide exerts anti-tumor activity in a wide range of cancer types through inhibition of a number of different pathways including Wnt, mTORC1, STAT3, NF-κB, and Notch (36–40). Functionally, niclosamide impairs tumor cell migration, invasion, and survival *in vitro* (41–42), and it reduces tumor growth *in vivo* (43,44). These results align with our findings supporting the notion that niclosamide is a multifunctional drug affecting a broad range of cellular pathways and functions. Importantly, in mouse models of breast, colon, and skin cancer, niclosamide treatment has led to reduced numbers of distant metastatic lesions (42–44), although the role of tumor cell extravasation across the endothelial barrier as a relevant mechanism was not investigated.

Our screen focused exclusively on endothelial barrier properties. We determined that exposure of endothelial monolayers to niclosamide prevented tumor cell extravasation by significantly enhancing transendothelial resistance levels, restoring barrier stability upon direct tumor cell-contact, and improving the cortical organization of actin cytoskeleton. Using a zebrafish model, we were able to directly visualize tumor cell extravasation *in vivo*, and to associate previously observed anti-tumor effects of niclosamide in mouse models to this particular step of the metastatic cascade. We also verified that niclosamide affected hematogenous metastasis. Importantly, exposure of the vasculature to niclosamide four days prior to tumor cell injection was sufficient to significantly impair lung colonization by tumor cells to levels similar to intervention trials. These findings in particular, underscore the concept that effects on vascular barrier stability are a significant component of the mechanism associated with niclosamide anti-metastatic effects.

Currently, based on its reportedly broad antitumor activity, niclosamide is being evaluated in 4 clinical trials for colon (Phase I, NCT02687009; Phase II, NCT02519582) and prostate cancer (Phase I, NCT03123978; Phase II, NCT02807805; ClinicalTrials.gov registry). In light of these ongoing trials, a timely understanding of the functional and molecular mechanisms of niclosamide in the context of the metastatic cascade is critical. In particular, both the proteomics and metabolomics evaluations performed here might prove valuable as biomarkers for molecular activity.

To shed light into the mechanistic underpinnings, gene expression profiles of tumor-endothelial cell co-cultures exposed to vehicle and niclosamide were determined at a single-cell level. Tumor-endothelial cell contact itself led to enrichment of gene annotations related to either inflammatory signaling, or cell-cell adhesion, intercellular junctions, and cytoskeletal regulation. Interestingly, the entire set of genes enhanced by niclosamide was enriched in annotations relevant to tumor cell extravasation. These included: cell-cell adhesion, adherens junctions, ECM organization, and actin cytoskeleton regulation. In addition, niclosamide affected multiple transcripts previously known to drive tumor cell extravasation. For example, niclosamide promoted substantial reductions in *CCL2* and *CXCL2* transcripts, both significantly upregulated upon initial tumor-endothelial contact. *In*

vivo binding of tumor cell-derived CCL2 to endothelial CCR2 facilitates tumor cell extravasation through endothelial retraction, induction of vascular permeability, and recruitment of monocytes (13,45). Likewise, CXCL2 secreted by endothelial cells induced endothelial barrier disruption by enhancing force generation and cytoskeletal dynamics of CXCR2 expressing tumor cells (46). Furthermore, niclosamide reduced the expression of tumor-derived matrix metallopeptidase 2 (*MMP2*) and von Willebrand factor (*VWF*), both molecules associated with tumor cell extravasation (47,48). A close evaluation of all ligand-receptor interactions impacted by niclosamide highlighted a key role for integrin beta-1 (*ITGB1*). In fact, *ITGB1* is critical for tumor cell extravasation, such as invadopodia formation, direct interaction with the subendothelial ECM, recruitment of F-actin at the protruding edge, and transmigration past the intercellular gaps of the endothelium (49). Accordingly, *ITGB1* has been reported to be crucial for tumor cell extravasation in a zebrafish and a chick embryo model, and plays a pro-metastatic role in different types of cancer (7,27). Using proteomics, we also noted that niclosamide treatment reduced kininogen levels, the precursor for bradykinin, which is a potent endothelium-dependent vasodilator and vascular permeability factor (50). The reduction in bradykinin is likely an important systemic contributor to the anti-metastatic effects mediated by niclosamide.

In light of novel immunotherapies for the treatment of solid tumors, the question arises how a drug impeding tumor cell extravasation would affect the trafficking of immune cells. The immature and leaky tumor vasculature substantially differs from the fairly healthy blood vessels in the pre-metastatic niche (51). In the context of immune cells that are highly specialized and well-equipped to transmigrate across the endothelial barrier (52), the prediction would be that drugs blocking tumor cell extravasation might not necessarily affect the well-orchestrated pathways used by immune cells. However, we have not investigated these aspects in depth at a molecular level, and future work on the effects of niclosamide on immune cell extravasation is needed.

In summary, our findings identify niclosamide as an effective drug for inhibition of tumor cell extravasation and hematogenous metastasis, highlighting its cell-specific properties and mechanistic effects. These results support the notion that drug-induced stabilization of cell-cell junctions and cell-matrix interactions attenuates the migratory and invasive capabilities of tumor cells, and simultaneously promotes endothelial barrier stabilization. Such drugs should be analyzed directly for their efficacy in human clinical settings, especially in association with surgical approaches which can enhance metastatic activity for short periods of time.

Supplementary Material

Refer to Web version on PubMed Central for supplementary material.

Acknowledgements

The authors thank Douglas Hanahan for providing the pancreatic cancer cell lines; Austin Quach for support with R; the UCLA Zebrafish Core Facility; Sequencing Core Facility; Broad Stem Cell Institute Flow Cytometry Core; Integrated Molecular Technologies Core. All high throughput screening experiments were performed at the UCLA Molecular Screening Shared Resource (supported by Comprehensive Cancer Center Grant NIH/NCI P30CA016042). Proteomics services were performed by the Northwestern Proteomics Core Facility, generously

supported by NCI CCSG P30 CA060553 awarded to the Robert H Lurie Comprehensive Cancer Center, instrumentation award (S10OD025194) from NIH Office of Director, and the National Resource for Translational and Developmental Proteomics supported by P41 GM108569. Metabolomics experiments were performed by the Metabolomics Core Facility at Feinberg School of Medicine at Northwestern University. This work was supported by NIH R01CA197943 and R35HL140014 to M.L. Iruela-Arispe, R01 HL140472 to J.-N. Chen, and a fellowship of the German Research Foundation (DFG; #HI1727/1-1) to G. Hilfenhaus and of the Sao Paulo Research Foundation (FAPESP; #2016/19968-3) to V. Freitas.

References

1. Steeg PS. Targeting metastasis. Nat. Rev. Cancer 2016;16:201–18. [PubMed: 27009393]
2. Neoptolemos JP, Kleeff J, Michl P, Costello E, Greenhalf W, Palmer DH. Therapeutic developments in pancreatic cancer: Current and future perspectives. Nat. Rev. Gastroenterol. Hepatol 2018;15:333–48. [PubMed: 29717230]
3. Martin OA, Anderson RL, Narayan K, MacManus MP. Does the mobilization of circulating tumour cells during cancer therapy cause metastasis? Nat. Rev. Clin. Oncol 2017;14:32–44. [PubMed: 27550857]
4. Kim MY, Oskarsson T, Acharyya S, Nguyen DX, Zhang XHF, Norton L, et al. Tumor Self-Seeding by Circulating Cancer Cells. Cell. 2009;139:1315–26. [PubMed: 20064377]
5. Joyce JA, Pollard JW. Microenvironmental regulation of metastasis. Nat. Rev. Cancer 2009;9:239–52. [PubMed: 19279573]
6. Strilic B, Offermanns S. Intravascular Survival and Extravasation of Tumor Cells. Cancer Cell. 2017;32:282–93. [PubMed: 28898694]
7. Reymond N, D'Água BB, Ridley AJ. Crossing the endothelial barrier during metastasis. Nat. Rev. Cancer 2013;13:858–70. [PubMed: 24263189]
8. Wettschureck N, Strilic B, Offermanns S. Passing the Vascular Barrier: Endothelial Signaling Processes Controlling Extravasation. Physiol Rev. 2019;99:1467–525. [PubMed: 31140373]
9. Dejana E Endothelial cell-cell junctions: happy together. Nat Rev Mol Cell Biol. 2004;5:261–70. [PubMed: 15071551]
10. Khuon S, Liang L, Dettman RW, Sporn PHS, Wysolmerski RB, Chew TL. Myosin light chain kinase mediates transcellular intravasation of breast cancer cells through the underlying endothelial cells: A three-dimensional FRET study. J Cell Sci. 2010;123(Pt3):431–40. [PubMed: 20067998]
11. Strilic B, Yang L, Albarrán-Juárez J, Wachsmuth L, Han K, Müller UC, et al. Tumour-cell-induced endothelial cell necroptosis via death receptor 6 promotes metastasis. Nature. 2016;536:215–8. [PubMed: 27487218]
12. Leong HS, Robertson AE, Stoletov K, Leith SJ, Chin CA, Chien AE, et al. Invadopodia Are Required for Cancer Cell Extravasation and Are a Therapeutic Target for Metastasis. Cell Rep. 2014;8:1558–70. [PubMed: 25176655]
13. Wolf MJ, Hoos A, Bauer J, Boettcher S, Knust M, Weber A, et al. Endothelial CCR2 Signaling Induced by Colon Carcinoma Cells Enables Extravasation via the JAK2-Stat5 and p38MAPK Pathway. Cancer Cell. 2012;22:91–105. [PubMed: 22789541]
14. Mierke CT. Endothelial cell's biomechanical properties are regulated by invasive cancer cells. Mol. Biosyst 2012;8:1639–49. [PubMed: 22498801]
15. Oldenburg J, De Rooij J. Mechanical control of the endothelial barrier. Cell Tissue Res. 2014;355:545–55. [PubMed: 24519624]
16. Aragon-Sanabria V, Pohler SE, Eswar VJ, Bierowski M, Gomez EW, Dong C. VE-Cadherin Disassembly and Cell Contractility in the Endothelium are Necessary for Barrier Disruption Induced by Tumor Cells. Sci Rep. 2017;7:45835. [PubMed: 28393886]
17. Martin TA, Jiang WG. Loss of tight junction barrier function and its role in cancer metastasis. Biochim. Biophys. Acta 2009;1788:872–91. [PubMed: 19059202]
18. La Porta SL, Roth L, Singhal M, Mogler C, Spegg C, Schieb B, et al. Endothelial Tie1–mediated angiogenesis and vascular abnormalization promote tumor progression and metastasis. J Clin Invest. 2018;128:834–45. [PubMed: 29355844]

19. Michael IP, Orebrand M, Lima M, Pereira B, Volpert O, Quaggin SE, et al. Angiopoietin-1 deficiency increases tumor metastasis in mice. BMC Cancer. 2017;17:539. [PubMed: 28800750]
20. Wieland E, Rodriguez-Vita J, Liebler SS, Mogler C, Moll I, Herberich SE, et al. Endothelial Notch1 Activity Facilitates Metastasis. Cancer Cell. 2017;31:355–367. [PubMed: 28238683]
21. Jean C, Chen XL, Nam J-O, Tancioni I, Uryu S, Lawson C, et al. Inhibition of endothelial FAK activity prevents tumor metastasis by enhancing barrier function. J Cell Biol. 2014;204:247–63. [PubMed: 24446483]
22. Wu FT, Lee CR, Bogdanovic E, Prodeus A, Gariépy J, Kerbel RS. Vasculotide reduces endothelial permeability and tumor cell extravasation in the absence of binding to or agonistic activation of Tie2. EMBO Mol Med. 2015;7:770–87. [PubMed: 25851538]
23. Blazejczyk A, Papiernik D, Porshneva K, Sadowska J, Wietrzyk J. Endothelium and cancer metastasis: Perspectives for antimetastatic therapy. Pharmacol. Reports. 2015;67:711–8.
24. Fontebasso Y, Dubinett SM. Drug development for metastasis prevention. Crit Rev Oncog. 2015;20:449–73. [PubMed: 27279241]
25. Hilfenhaus G, Nguyen DP, Freshman J, Prajapati D, Ma F, Song D, et al. Vav3-induced cytoskeletal dynamics contribute to heterotypic properties of endothelial barriers. J Cell Biol. 2018;217:2813–30. [PubMed: 29858212]
26. Choi J, Dong L, Ahn J, Dao D, Hammerschmidt M, Chen JN. FoxH1 negatively modulates flk1 gene expression and vascular formation in zebrafish. Dev Biol. 2007;304:735–44. [PubMed: 17306248]
27. Stoletov K, Kato H, Zardouzian E, Kelber J, Yang J, Shattil S, et al. Visualizing extravasation dynamics of metastatic tumor cells. J Cell Sci. 2010;123(Pt13):2332–41. [PubMed: 20530574]
28. Wang Y, Wang R, Zhang S, Song S, Jiang C, Han G, et al. iTALK: an R package to characterize and illustrate intercellular communication. 2019;bioRiv doi:10.1101/507871. 1 2019, preprint: not peer reviewed.
29. Cox J, Hein MY, Luber CA, Paron I, Nagaraj N, Mann M. Accurate Proteome-wide Label-free Quantification by Delayed Normalization and Maximal Peptide Ratio Extraction, Termed MaxLFQ. Mol Cell Proteomics. 2014;13:2513–26. [PubMed: 24942700]
30. Tyanova S, Temu T, Sinitcyn P, Carlson A, Hein MY, Geiger T, et al. The Perseus computational platform for comprehensive analysis of (prote)omics data. Nat Methods. 2016;13:731–40. [PubMed: 27348712]
31. Zhang JH, Chung TDY, Oldenburg KR. A simple statistical parameter for use in evaluation and validation of high throughput screening assays. J Biomol Screen. 1999;4:67–73. [PubMed: 10838414]
32. Flatau G, Lemichez E, Gauthier M, Chardin P, Paris S, Fiorentini C, et al. Toxin-induced activation of the G protein p21 Rho by deamidation of glutamine. Nature. 1997;387:729–33. [PubMed: 9192901]
33. Ortega MC, Santander-García D, Marcos-Ramiro B, Barroso S, Cox S, Jiménez-Alfaro I, et al. Activation of Rac1 and Rhoa preserve corneal endothelial barrier function. Investig Ophthalmol Vis Sci. 2016;57:6210–22. [PubMed: 27849309]
34. Fukuhara S, Sakurai A, Sano H, Yamagishi A, Somekawa S, Takakura N, et al. Cyclic AMP Potentiates Vascular Endothelial Cadherin-Mediated Cell-Cell Contact To Enhance Endothelial Barrier Function through an Epac-Rap1 Signaling Pathway. Mol Cell Biol. 2005;25:136–46. [PubMed: 15601837]
35. Chen W, Mook RA, Premont RT, Wang J. Niclosamide: Beyond an antihelminthic drug. Cell. Signal. 2018;41:89–96. [PubMed: 28389414]
36. Fonseca BD, Diering GH, Bidinosti MA, Dalal K, Alain T, Balgi AD, et al. Structure-activity analysis of niclosamide reveals potential role for cytoplasmic pH in control of mammalian target of rapamycin complex 1 (mTORC1) signaling. J Biol Chem. 2012;287:17530–45. [PubMed: 22474287]
37. Ren X, Duan L, He Q, Zhang Z, Zhou Y, Wu D, et al. Identification of niclosamide as a new small-molecule inhibitor of the STAT3 signaling pathway. ACS Med Chem Lett. 2010;1:454–59. [PubMed: 24900231]

38. Jin Y, Lu Z, Ding K, Li J, Du X, Chen C, et al. Antineoplastic mechanisms of niclosamide in acute myelogenous leukemia stem cells: Inactivation of the NF-κB pathway and generation of reactive oxygen species. Cancer Res. 2010;70:2516–27. [PubMed: 20215516]
39. Chen M, Wang J, Lu J, Bond MC, Ren XR, Lyerly HK, et al. The anti-helminthic niclosamide inhibits Wnt/Frizzled1 signaling. Biochemistry. 2009;48:10267–74. [PubMed: 19772353]
40. Wang J, rong Ren X, Piao H, Zhao S, Osada T, Premont RT, et al. Niclosamide-induced Wnt signaling inhibition in colorectal cancer is mediated by autophagy. Biochem J. 2019;476:535–46. [PubMed: 30635359]
41. Yu K, Wang T, Li Y, Wang C, Wang X, Zhang M, et al. Niclosamide induces apoptosis through mitochondrial intrinsic pathway and inhibits migration and invasion in human thyroid cancer in vitro. Biomed Pharmacother. 2017;92:403–11. [PubMed: 28575805]
42. Sack U, Walther W, Scudiero D, Selby M, Kobelt D, Lemm M, et al. Novel effect of antihelminthic niclosamide on s100a4-mediated metastatic progression in colon cancer. J Natl Cancer Inst. 2011;103:1018–36. [PubMed: 21685359]
43. Ye T, Xiong Y, Yan Y, Xia Y, Song X, Liu L, et al. The anthelmintic drug niclosamide induces apoptosis, impairs metastasis and reduces immunosuppressive cells in breast cancer model. PLoS One. 2014;9:e85887. [PubMed: 24416452]
44. Zhu Y, Zuo W, Chen L, Bian S, Jing J, Gan C, et al. Repurposing of the anti-helminthic drug niclosamide to treat melanoma and pulmonary metastasis via the STAT3 signaling pathway. Biochem Pharmacol. 2019;169:113610. [PubMed: 31465777]
45. Roblek M, Protsyuk D, Becker PF, Stefanescu C, Gorzelanny C, Glaus Garzon JF, et al. CCL2 is a vascular permeability factor inducing CCR2-dependent endothelial retraction during lung metastasis. Mol Cancer Res. 2019;17:783–793. [PubMed: 30552233]
46. Mierke CT, Zitterbart DP, Kollmannsberger P, Raupach C, Schlötzer-Schrehardt U, Goecke TW, et al. Breakdown of the endothelial barrier function in tumor cell transmigration. Biophys J. 2008;94:2832–46. [PubMed: 18096634]
47. Shen Q, Lee ES, Pitts RL, Wu MH, Yuan SY. Tissue inhibitor of metalloproteinase-2 regulates matrix metalloproteinase-2-mediated endothelial barrier dysfunction and breast cancer cell transmigration through lung microvascular endothelial cells. Mol Cancer Res. 2010;8:939–51. [PubMed: 20571065]
48. Mojiri A, Stoletov K, Carrillo MAL, Willetts L, Jain S, Godbout R, et al. Functional assessment of von Willebrand factor expression by cancer cells of non-endothelial origin. Oncotarget. 2017;8:13015–29. [PubMed: 28035064]
49. Chen MB, Lamar JM, Li R, Hynes RO, Kamm RD. Elucidation of the roles of tumor integrin β1 in the extravasation stage of the metastasis cascade. Cancer Res. 2016;76:2513–24. [PubMed: 26988988]
50. Kaplan AP, Ghebrehiwet B. The plasma bradykinin-forming pathways and its interrelationships with complement. Mol Immunol. 2010;47:2161–9. [PubMed: 20580091]
51. Peinado H, Zhang H, Matei IR, Costa-Silva B, Hoshino A, Rodrigues G, et al. Pre-metastatic niches: organ-specific homes for metastases. Nat Rev Cancer. 2017;17:302–17. [PubMed: 28303905]
52. Strell C, Entschladen F. Extravasation of leukocytes in comparison to tumor cells. Cell Commun Signal. 2008;6:10. [PubMed: 19055814]

Significance

A high-content screen identified niclosamide as an effective drug that restricts tumor cell extravasation by enhancing endothelial barrier stability through modulation of molecular signaling, chemokines, and tumor-endothelial cell interactions.

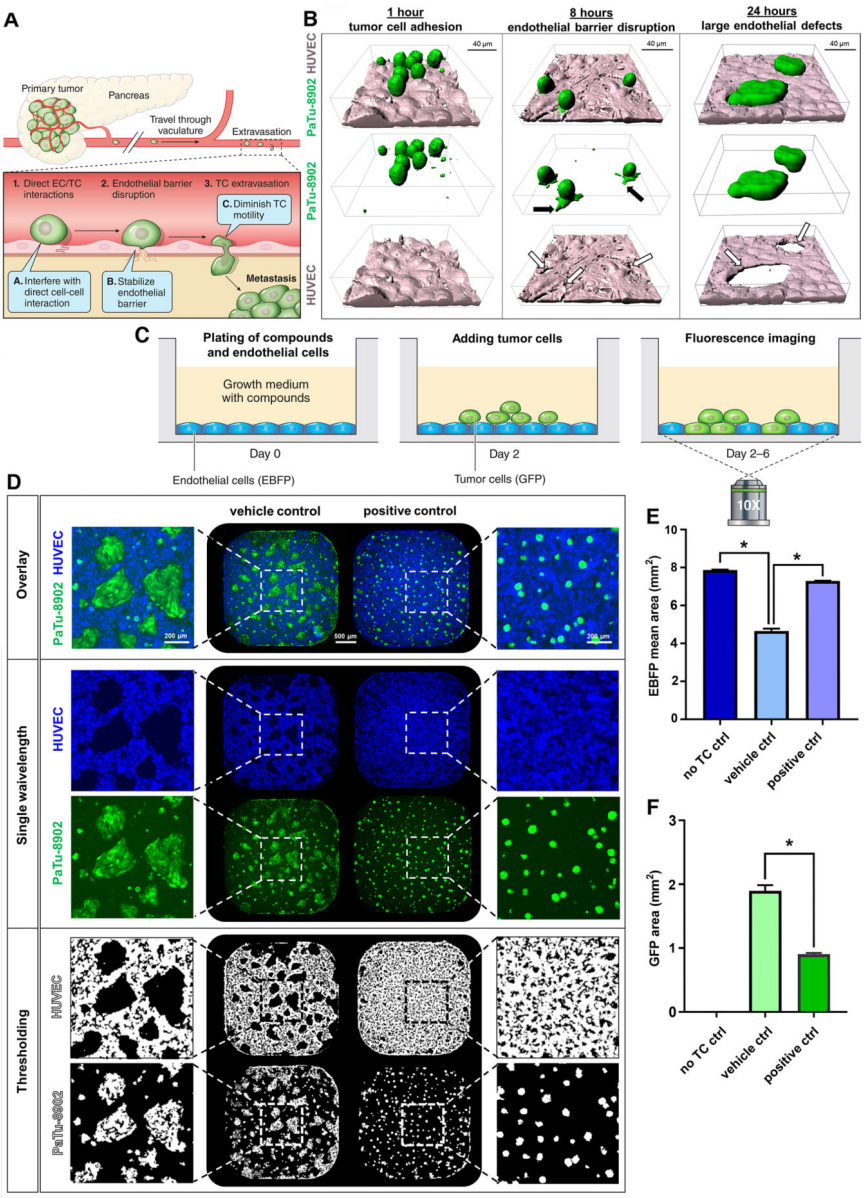

Figure 1: A high-content screening assay to identify compounds that prevent transendothelial tumor cell invasion.

A Illustration highlighting the consecutive steps of tumor cell extravasation that result in distant metastases. In the primary tumor, invasive cancer cells enter the vascular system and travel to distant organ sites, where they directly adhere to (1) and disrupt (2) the endothelial barrier, to transmigrate into the extravascular space (3). Compounds that either interfere with the early direct tumor-endothelial cell interactions (A), stabilize the endothelial barrier (B), or target tumor cell motility / invasiveness (C) bear promising characteristics to prevent tumor cell extravasation. **B** 3-D surface rendering of human pancreatic cancer cells (PaTu-8902) that adhere to, destabilize, and invade a monolayer of human endothelial cells (HUVECs) during a 24-hour time course. This represents an *in vitro* model for transendothelial tumor cell invasion. At 8 hours, protrusions of tumor cells (filled arrows) induce intercellular gaps in the endothelial monolayer (open arrows), enabling tumor cells to

fully invade the monolayer (open arrows, 24 hours). **C** Workflow of the high-content screening assay using a 384-well format. EBFP-labeled HUVECs are plated with growth medium and compounds (day 0). GFP-labeled pancreatic cancer cells are added on top of the HUVEC monolayer (day 2), and fluorescence imaging of the entire well is performed every 24 hours (day 2–6). **D** Overlay and single wavelength fluorescence images of 384-wells and magnifications taken 3 days after plating of PaTu-8902 onto HUVEC monolayers treated either with vehicle control or positive control substance (CN03). Thresholding of blue and green fluorescence is used for quantification of HUVEC and PaTu-8902 total areas, respectively. **E** Total area of HUVEC monolayers (EBFP) per 384-well without tumor cells (negative control), and co-cultured with PaTu-8902 treated either with vehicle control, or positive control CN03 (as images shown in D; mean±SEM; *P<0.05; n=3). **F** Total GFP-positive area of negative control wells, and PaTu- 8902 co-cultures treated with either vehicle control, or positive control CN03 (mean±SEM; *P<0.05; n=3).

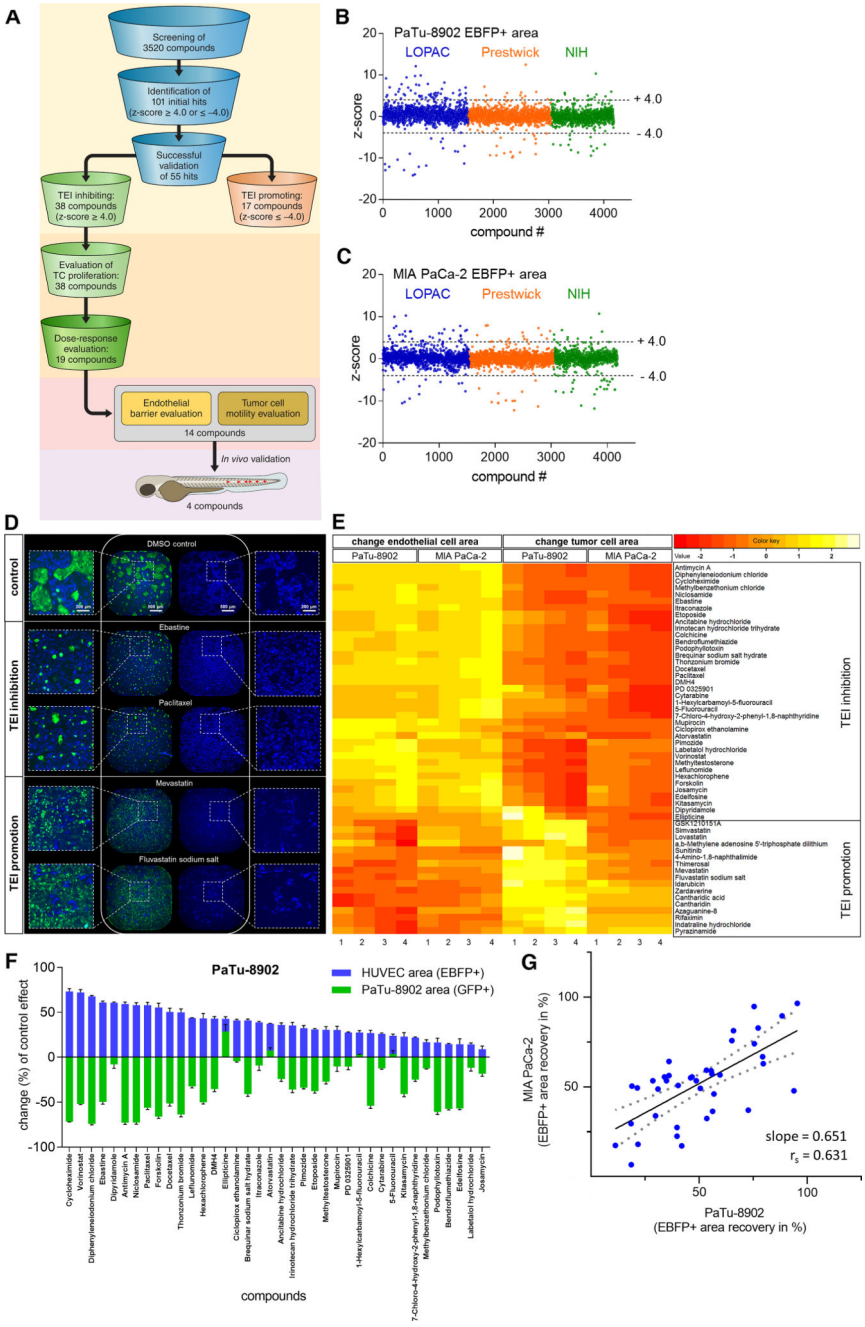

Figure 2: High-content screen identifies compounds that impair transendothelial invasion of pancreatic cancer cells *in vitro*.

A Shown is the high-content screening and compound validation workflow. By screening a total of 3520 compounds, and detection of 101 initial assay hits, 55 compounds were finally identified of which 38 reduced (z-score ≥ 4.0; EBFP-positive area), and 17 promoted transendothelial invasion (TEI; z-score ≤ −4.0; EBFP-positive area). Elimination of compounds with large effects on tumor cell proliferation (38 compounds tested) and high EC50 values (dose-response evaluation; 19 compounds tested) sifts out 14 compounds with promising characteristics (Fig. 3). Further evaluation of effects on endothelial barrier

function and tumor cell motility highlights 4 compounds (Suppl. Fig. 4) which are further validated *in vivo* using a zebrafish model (Fig. 4). **B, C** EBFP-positive area distribution (z-score) of all 3520 screened compounds as part of the libraries LOPAC^{1280} (LOPAC), Prestwick Chemical Library (Prestwick), and NIH Clinical Collection (NIH) using the transendothelial tumor cell invasion assay with PaTu-8902 (B), or MIA PaCa-2 (C, hits defined as z-score ≥ 4.0, or ≤ −4.0; imaging on day 3 post tumor cell addition). **D** Representative fluorescence images showing effects of two transendothelial invasion (TEI) inhibiting compounds (ebastine, and paclitaxel), and two transendothelial invasion promoting compounds (mevastatin, and fluvastatin sodium salt) versus DMSO control for PaTu-8902 (images show entire 384-wells and magnifications, respectively). **E** Hierarchical clustering heatmap summarizing results obtained for the 55 hits that were successfully validated in triplicates across 4 different imaging timepoints (shown are EBFP- and GFP-positive areas 1–4 days after addition of either PaTu-8902, or MIA PaCa-2). Compounds reducing (upper) and promoting (lower) transendothelial invasion (TEI) are shown. **F** Quantification of HUVEC (EBFP-positive) and PaTu-8902 areas (GFP-positive) obtained for all compounds inhibiting transendothelial invasion (validated in triplicates; results shown as mean ± SEM of %-change to DMSO controls). **G** Correlation of restored HUVEC area (EBFP-positive) for PaTu-8902 versus MIA PaCa-2 per compound inhibiting transendothelial invasion (shown is best-fit line with 95% confidence bands; slope = 0.651; $r_s = 0.631$, $p<0.0001$).

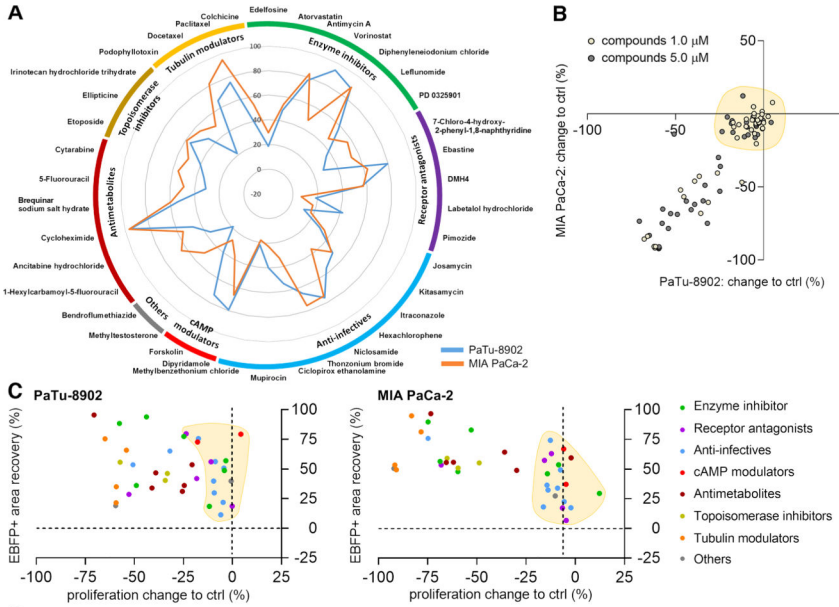

D

	PaTu-8902		MIA PaCa-2	
compounds	*EC50 (µM)*	*SEM*	*EC50 (µM)*	*SEM*
Diphenyleneiodonium chloride	0.05	0.01	0.10	0.01
Niclosamide	0.30	0.03	0.54	0.05
Atorvastatin	0.43	0.06	4.01	0.49
Dipyridamole	0.55	0.06	3.10	0.30
Edelfosine	0.75	0.13	2.40	0.41
Hexachlorophene	1.34	0.18	2.24	0.23
Kitasamycin	1.51	0.20	3.15	0.35
DMH4	2.29	0.24	3.08	0.25
Ebastine	3.00	0.39	6.52	0.63
Forskolin	3.23	0.43	7.40	0.82
Josamycin	4.69	0.75	10.15	0.82
Methylbenzethonium chloride	5.43	0.87	5.50	0.86
Itraconazole	6.55	2.25	4.00	0.71
Mupirocin	9.53	1.29	12.79	1.33

Figure 3: Effects on transendothelial invasion and tumor cell proliferation by drug category, and dose-response evaluation.

A Radar plot illustrating the effects of validated compounds on transendothelial invasion for both PaTu-8902 and MIA PaCa-2 grouped by drug categories (% of EBFP-positive area recovery to DMSO control). **B** Effects on tumor cell proliferation of identified compounds at 1.0 µM and 5.0 µM shown as correlation of PaTu-8902 versus MIA PaCa-2. Compounds with minor or no effect on tumor cell proliferation that were chosen for further in vitro validation are shaded in yellow. **C** Impact on PaTu-8902 and MIA PaCa-2 transendothelial invasion in relation to effects on tumor cell proliferation by compound and drug categories (as highlighted in different colors). Compounds with limited effects on proliferation are shaded in yellow and were selected for further dose-response evaluation. **D** Shown are compounds with EC50 values ≤ 10 µM for PaTu-8902 obtained by dose-response evaluation (values are shown for both PaTu-8902 and MIA PaCa-2; mean±SEM).

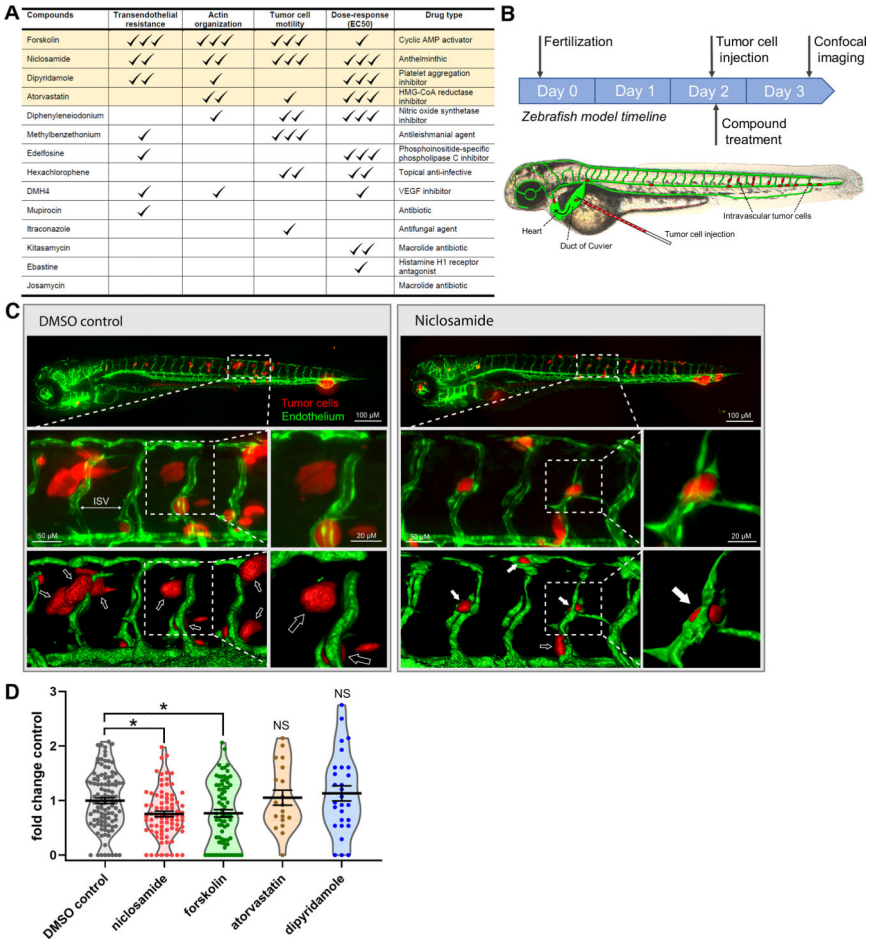

Compounds	Transendothelial resistance	Actin organization	Tumor cell motility	Dose-response (EC50)	Drug type
Forskolin	✓✓✓	✓✓✓	✓✓✓	✓	Cyclic AMP activator
Niclosamide	✓✓	✓✓	✓✓✓	✓✓✓	Anthelmintic
Dipyridamole	✓✓	✓		✓✓✓	Platelet aggregation inhibitor
Atorvastatin		✓✓	✓	✓✓✓	HMG-CoA reductase inhibitor
Diphenyleneiodonium		✓	✓✓	✓✓✓	Nitric oxide synthetase inhibitor
Methylbenzethonium	✓		✓✓✓		Antileishmanial agent
Edelfosine	✓			✓✓✓	Phosphoinositide-specific phospholipase C inhibitor
Hexachlorophene			✓✓	✓✓	Topical anti-infective
DMH4	✓	✓		✓	VEGF inhibitor
Mupirocin	✓				Antibiotic
Itraconazole			✓		Antifungal agent
Kitasamycin				✓✓	Macrolide antibiotic
Ebastine				✓	Histamine H1 receptor antagonist
Josamycin					Macrolide antibiotic

Figure 4: Niclosamide and forskolin impair tumor cell extravasation in zebrafish.

A Table summarizing the *in vitro* performance of the top 14 compounds. Compounds were graded with up to 3 check marks depending on the magnitude of the observed effect for each *in vitro* assay. Four compounds (forskolin, niclosamide, dipyridamole, and atorvastatin) were selected for further *in vivo* validation (shaded in beige). **B** Timeline and technical approach of the zebrafish tumor cell extravasation model. 2 days post fertilization (dpf) tumor cells were injected into the precardiac sinus of *Tg(kdrl:GFP)*^{la116} zebrafish embryos, treatment with compounds addred into the fish water. 30 hours post tumor cell injection (3 dpf) 3-D spinning disc confocal imaging was performed. See Suppl. Fig. 5 B for further details regarding the zebrafish validation platform. **C** Upper image shows representative maximum intensity images of zebrafish treated with either DMSO control or niclosamide (1.0 μM) 30 hours post intravascular injection of RFP-labeled PaTu-8902. Lower images showed magnifications of intersegmental vessels (ISV) and 3-D surface renderings (lower images). Open arrows point to extravascular PaTu-8902; filled arrows highlight intravascular tumor cells. **D** Scatter-violin plot showing fold-change of extravascular tumor cell percentage per zebrafish grouped by compound treatment (niclosamide 1.0 μM, forskolin 0.5 μM, atorvastatin 2.0 μM, dipyridamole 2.0 μM) versus DMSO control (*, $P < 0.05$ vs. control; mean ± SEM).

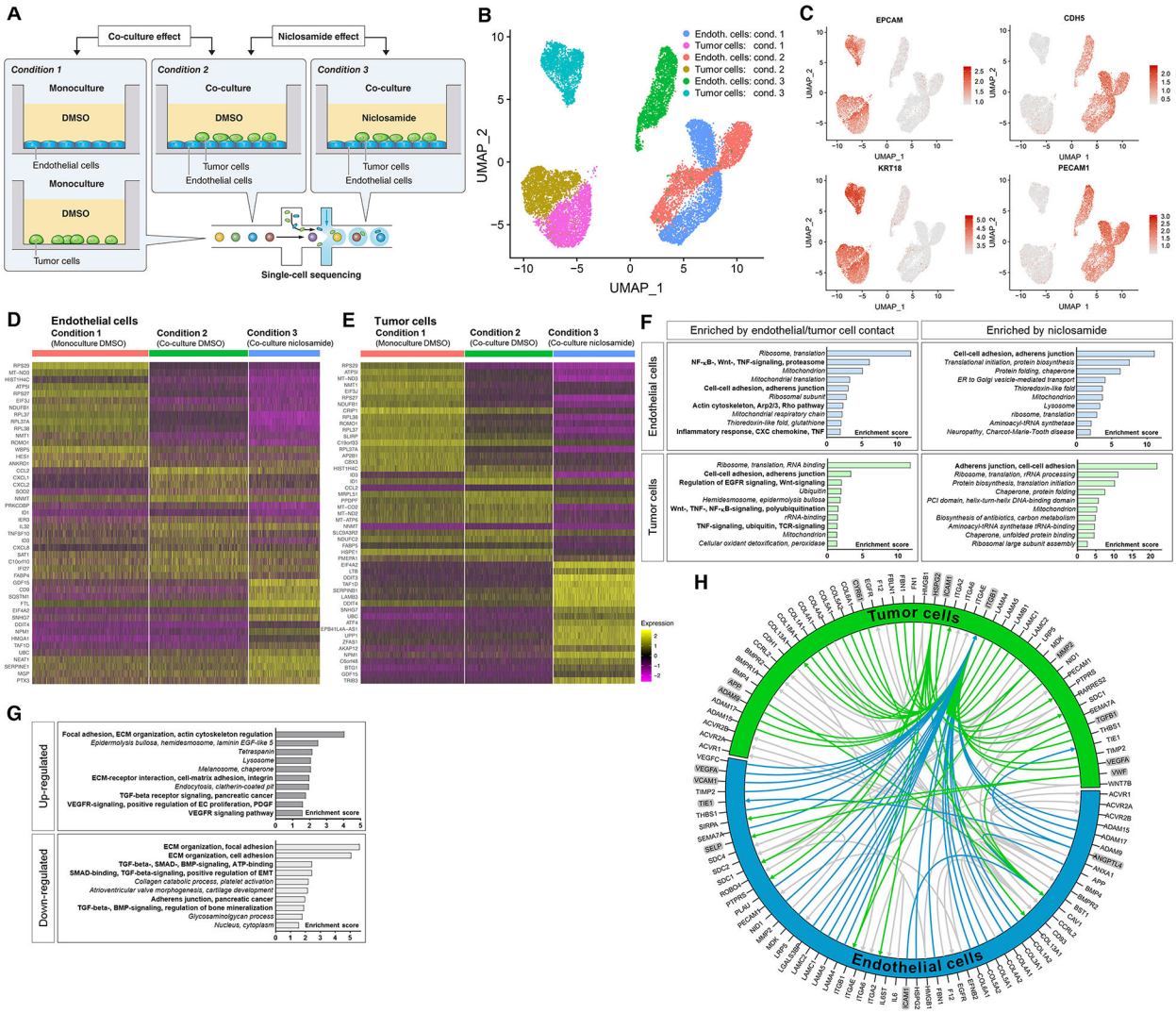

Figure 5: Niclosamide modulates cell-cell / cell-matri regulatory networks and endothelial barrier stability.

A Experimental design used for single-cell sequencing. To assess effects of direct tumor-endothelial contact versus monoculture, PaTu-8902 and HUVECs were either cultured in separate wells (condition 1), or PaTu-8902 was plated on top of a confluent monolayer of HUVECs (condition 2) over 8 hours, both in the presence of DMSO (vehicle control). To assess the effect of niclosamide on both cell types during co-culture, each cell type alone or together were treated with 1.0 uM niclosamide over the course of 8 hours (condition 3; following a 12- hour niclosamide pretreatment of the HUVEC monolayer). **B** UMAP-plot highlights each cell type and experimental condition based on distinct RNA expression profiles (Endoth. cells = HUVEC; Tumor cells = PaTu-8902). **C** UMAP-plot showing expression of cell-specific markers which define endothelial cell (CDH5, PECAM1), and tumor cell (EPCAM, KRT19) identity. **D, E** Heatmaps of genes with most significant changes of RNA-expression levels per sample condition shown for HUVEC (D) and PaTu-8902 (E). **F** Enriched functional gene annotation clusters of all identified genes that were upregulated by either tumor-endothelial cell contact, or niclosamide treatment in

HUVEC and PaTu-8902, respectively (clusters that are relevant for tumor cell extravasation are shown in bold; generated using DAVID Bioinformatics resources). **G** Enriched functional gene annotation clusters of all ligand-receptor interactions that are up- or downregulated by niclosamide treatment in the HUVEC / PaTu-8902 co-culture (clusters that are relevant for tumor cell extravasation are shown in bold). **H** Circos plot showing the ligand- receptor interactions that are part of the top downregulated functional gene annotation cluster “ECM organization, focal adhesion” (as shown in G). Genes that have been associated with tumor cell extravasation in the current literature are highlighted in grey. Their interactions are shown in blue (endothelial cell ligand) or green (tumor cell ligand) with the arrow pointing to its corresponding receptor.

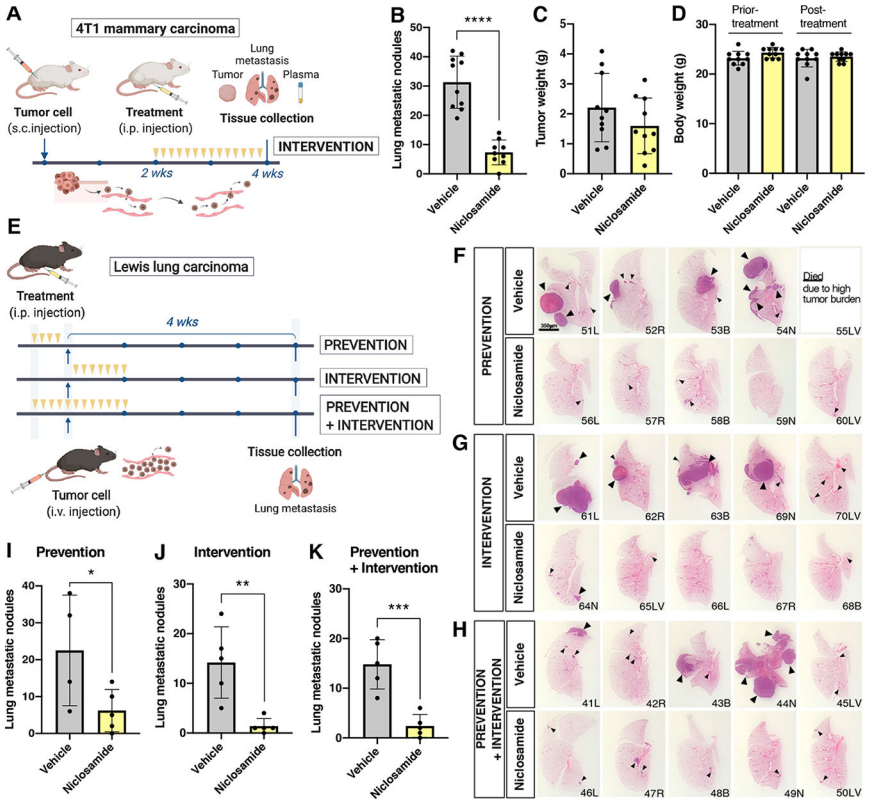

Figure 6: Niclosamide suppresses metastatic spreading in syngeneic mouse models.

A Experimental design followed for metastatic assays using 4T1 mammary carcinoma cells in BalbC mice. Mice were injected subcutaneously, tumors were allowed to grow for two weeks, at which time mice were randomized and treated daily with either vehicle or niclosamide for two additional weeks. **B** Quantification of lung metastasis performed by counting fluorescently-labeled tumor nodules in the entire right lung lobe (n=10mice/group). **C** Tumor weight at the termination of the experiment shows no statistically difference between groups. **D** Total animal weight prior and post-treatment shows no detrimental effect of niclosamide treatment. **E** Experimental design followed for metastatic assays using LLC cells in C57Bl6J mice. Three groups (prevention, intervention and prevention+intervention) were treated with niclosamide or vehicle as indicated (yellow arrows)(n=5 per group). **F, G, H** H&E images of the left lung lobe to illustrate size and distribution of tumor nodules in the three treatment groups. Bar= 3.5mm. **I, J, K** Bar graph of lung metastatic nodules counted on vibratome sections of the right lung lobe by two individuals blinded to the treatments (n=5 per group). Statistics Unpaired t test (two-tail). (*P < 0.05, **P < 0.01, ***P < 0.001, mean ± SD).

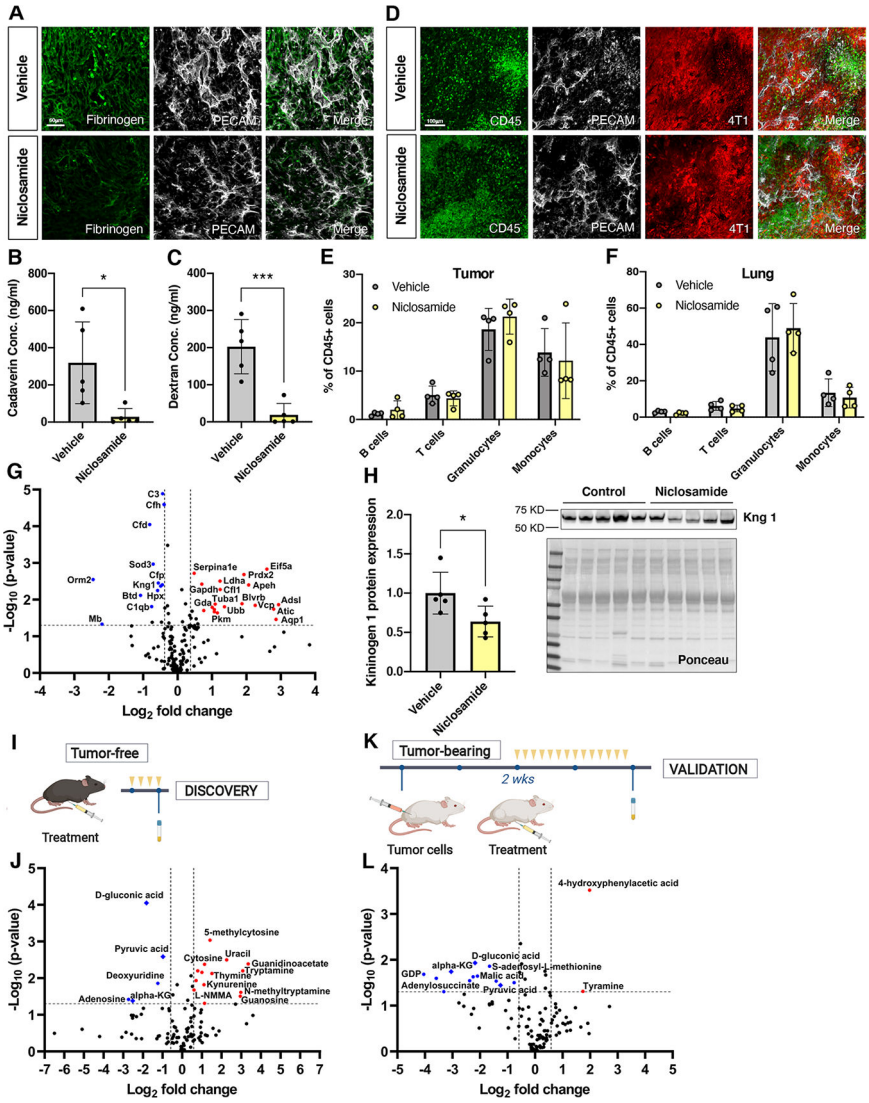

Figure 7: Niclosamide inhibits permeability but does it not affect trafficking of immune cells.

A Immunocytochemistry for fibrinogen (green) in primary tumors (4T1) treated with vehicle or niclosamide. PECAM (white) was used as an endothelial marker. Bar= 60um **B** Bar graph showing cadaverin (1kDa) extravasation in the lung of tumor-bearing mice treated with either vehicle or niclosamide (unpaired t test) (*P < 0.05) **C** Bar graph showing dextran (10kDa) extravasation in the lung of tumor-bearing mice treated with either vehicle or niclosamide normalized to tissue weight (unpaired t test) (***P < 0.001) **D** Immunocytochemistry of CD45+ cells (green) in primary tumors, vessels were identified by PECAM (white) and tumor cells by expression of Tdtomato (red). **E, F** Bar graph of leukocytes expressed as percentage of total cells in primary tumor (E) and lung (F) treated with niclosamide and vehicle. **G** Volcano plot representing the distribution of 172 plasma proteins with their relative protein abundance after non-tumor bearing animals were exposed to niclosamide and in relation to vehicle exposed animals. Statistically significant proteins were determined by t-test using a permutation-based FDR method for multiple hypothesis corrections using LFQ intensity derived by MaxQuant. Significantly up (n=19)- and down

(n=13)-regulated proteins in *Niclo* group are highlighted in red and blue, respectively. Analysis was done in plasma from n=3 mice per group. **H** Validation of kininogen in tumor-bearing animals exposed to vehicle or niclosamide was done by Western blot of plasma proteins. The graph shows quantification of the Western blot on the right. Ponceau staining of the transfer provides an assessment of protein loading levels (n=5 per group). **I** Experimental design for metabolomic analyses of tumor-free mice with niclosamide or vehicle. **J** Volcano plot of metabolomics performed on plasma of tumor-free mice analyzed by HPLC-MS/MS and analyzed in Xcalibur4 (n=3 per group). **K** Experimental design for validation of the metabolomic analyses. Treated with niclosamide or vehicle is indicated by the yellow arrowheads. **L** Volcano plot of metabolomics from the plasma of tumor-bearing mice analyzed by HPLC-MS/MS and analyzed in Xcalibur4. Diamond shaped symbols indicate metabolites that overlapped in tumor free- and tumor-bearing mice (n=8 per group).